Electronic Supplementary Information

Origin of the Superior Oxygen Reduction Activity of Zirconium Nitride in Alkaline Media

Heng Liu [a, b], *Di Zhang* [a], *Stuart M. Holmes* [b], *Carmine D'Agostino* [b,c,*], *and Hao Li* [a,*]

[a] *Advanced Institute for Materials Research (WPI-AIMR), Tohoku University, Sendai 980-8577, Japan*

[b] *Department of Chemical Engineering, The University of Manchester, Oxford Road, M13 9PL, UK*

[c] *Dipartimento di Ingegneria Civile, Chimica, Ambientale e dei Materiali (DICAM), Alma Mater Studiorum – Università di Bologna, Via Terracini, 28, 40131 Bologna, Italy*

*** Correspondence:**

carmine.dagostino@manchester.ac.uk (C.D.)

li.hao.b8@tohoku.ac.jp (H.L.)

Computational and Modeling Details

The Vienna *ab initio* simulation package (VASP) [1] employing the projector augmented wave (PAW) method [2, 3] was used for the spin-polarized density functional theory (DFT) calculations. Valence electrons were described by the Kohn-Sham wave functions [4] which are expanded in a plane-wave basis set [3] with a kinetic energy cutoff of 520 eV. Convergence criteria for geometric relaxation was referred to the forces acting on each atom less than 0.03 eV/Å. Electron exchange and correlation interactions were calculated using the general gradient approximation (GGA) [5] method parametrized by the revised Perdew–Burke–Ernzerhof (RPBE) functional [6]. A (3×3×1) *k*-point mesh was used to sample the Brillouin zone [7] and a vacuum slab of 15 Å was chosen in the *z*-direction to separate two periodic surfaces. For the binding energy calculations, the bottom two layers were fixed to the bulk positions while the rest layers were allowed to relax. The Python Materials Genomics (pymatgen) [8] and Atomic Simulation Environment (ASE) [9] Libraries were introduced to manipulate the crystal structure, generate inputs, and compare the surface stability. The computational parameters for bulk structures were referred to the *Materials Project* database [10]. Prior to the study, stricter computational methods were evaluated, including larger kinetic energy cutoff, larger *k*-point mesh grid, lower convergent force, thicker layer, and larger unit cell. In the course of conducting these tests, only the variable of interest was manipulated during each test while all other parameters were maintained at constant levels (note: the functional was fixed at RPBE). However, no significant difference was observed in the binding energies and the optimized adsorption geometries. The surface Pourbaix diagrams' energetics were computed using the computational hydrogen electrode (CHE) method proposed by Nørskov et al. [11] as a function of pH and potential. The zero-point energy (ZPE) and entropic corrections were obtained from a previous study [12] at 298.15 K. Solvation corrections were implemented for the HO* species, as the strong hydrogen bonding effects result in additional stabilization of bonding strengths. The values for these corrections were obtained from Refs. [12, 13]. The water dissociation equilibrium during electrocatalysis is shown below:

$$H_nO_m^* + (2m - n)(H^+ + e^-) \rightleftarrows * + mH_2O, (1)$$

where m and n denote the number of O and H adsorbed on a pristine surface, respectively. The free energies of every surface state in the surface Pourbaix diagram (G_{SP}) can be calculated by:

$$G_{SP} = G_{bare} + mG_{H_2O} - G_{tot} - (2m - n)({}^1\!/_2G_{H_2} - U_{SHE} - 2.303k_BT * pH), (2)$$

where G_{bare}, G_{H_2O}, G_{tot}, and G_{H_2} denote the total energies of the pristine surface, a water molecule, the surface with adsorbates, and a hydrogen molecule. U_{SHE} represents the potential referenced to standard hydrogen electrode (SHE) while k_B is the Boltzmann constant, and T is the temperature (at 298.15 K). To evaluate the most energetically stable stoichiometric surface, the surface energies (E_{Surf}) were computed using the following equation:

$$E_{Surf} = \frac{E_{Slab} - dE_{Bulk}}{2S}, (3)$$

in which E_{Slab} and E_{Bulk} are the total energies of the slab cleaved from the bulk structure and bulk models. Atomic ratio between the slab and the bulk is denoted by d. S is the area of the surface. Adsorption energy ΔG of different intermediates (denoted as *ads*) on the calculated surface can be defined as:

$$\Delta G = \Delta E + \Delta ZPE - T\Delta S, (4)$$

$$\Delta E = E_{*-ads} - E_* - E_{ads}, (5)$$

where E_{*-ads}, E_*, and E_{ads} denote total energies for surface with adsorbates, clean surface, and the adsorbate (the energy was calculated referred to water and hydrogen molecule).

Electric field effects simulation methods

Electric fields (EF) were introduced based on the methods proposed by Kelly et al. [14] using a saw-tooth potential corresponding to fields between -0.8 and 0.8 V^{-1}. Calculations concerning the electric field were performed *via* the Quantum Espresso code [15]. The input parameters were referring to those employed in VASP including GGA, KPOINTS, vacuum layer thickness, *etc*. To ensure the accuracy of the computational models, the electronic structure information of the same model using VASP and Quantum Espresso is given out in **Figure S3**. No significant difference is observed. Surface adsorption species were allowed to relax under each electric field. It was hypothesized that the ZPE, entropy, and solvation corrections remained constant for all field values. Transition state (TS) involving in the ORR were also considered to hold a similar responding to the electric field as the initial state (IS), so μ and α (in Equation 10) were set at the same values for both IS and TS. Then, the parallel-plate capacitor model was applied to calculate the EF *via* Equation 6 with the PZC set to 0, in which σ refers to charge density, 0 refers to vacuum permittivity (8.85 * 10^{-12} F m^{-1}), ε denotes dielectric constant (unitless), and C_H is the Helmholtz capacitance (μF cm^{-2}).

$$\vec{E} = \frac{\sigma}{\varepsilon\varepsilon_0} = \frac{C_H(U_{SHE} - U_{PZC})}{\varepsilon\varepsilon_0} = \frac{C_H * U_{SHE}}{\varepsilon\varepsilon_0}, \quad (6)$$

$$U_{SHE} = U_{RHE} - k_B T \ln(10) \times pH. \quad (7)$$

Besides, it is a common sense that U_{SHE} and U_{RHE} differ only by pH as shown in Equation 7. By combining these two equations, it becomes evident that the pH value can be predicted by the electric field. An increase in pH would result in a more negative electric field, while a decrease in pH would lead to a more positive electric field.

Based on the results from Kelly et al. [14], we set ε as 2 and C_H as a constant of 25 μF cm^{-2}. A second order polynomial was fitted to monitor the adsorbates' response to the

EF and values are considered for intrinsic dipole moment (μ) and polarizability (α). The equation is as below:

$$G_{ads} = G^{\vec{E}=0}_{ads} + \mu\vec{E} - \frac{\alpha}{2}\vec{E}^2, (8)$$

where $G^{\vec{E}=0}_{ads}$ is the binding energy of an adsorbate computed without external electric field. The CHE was used to correct binding energy for RHE dependence in Equation 9, where n denotes number of electrons and e refers to the charge of a single electron.

$$G_{ads} = G_{ads,U_{RHE}=0} - neU_{RHE}. (9)$$

Ultimately, we can obtain the information of binding energies corresponding to different electric fields scaled in the RHE criteria:

$$G_{ads} = G^{\vec{E}=0}_{ads} + \mu\vec{E} - \frac{\alpha}{2}\vec{E}^2 - neU_{RHE}. (10)$$

Microkinetic modelling method

The advanced microkinetic models coupling with electric field effects was referred to the methods by Hansen et al. [16] and Kelly et al. [14] in the CatMAP [17] package. This method adopts the results from the scaling relationship and electric field simulation to generate the polarization curves and the pH-dependent volcano plots.

The steady-state approximation method was employed to decide the adsorbate coverages. The rates for intermediate steps were calculated by the following equation:

$$rate = k_f\prod\theta_{reac} - k_r\prod\theta_{prod}, (11)$$

here, $k = AExp[-\frac{G_a}{k_BT}]$, where A is the reaction prefactor in s^{-1}, and G_a is the activation free energy. θ_{reac} and θ_{prod} are the coverage of reactants and products, respectively.

The intermediate reactions considered in the modeling are shown in the following Reactions:

$$O_2(aq) \rightarrow O_2(dl), (12)$$

$O_2(dl) + * \rightarrow O_2^*$, (13)

$O_2^* + (H^+ + e^-) + * \rightarrow HOO^*$, (14)

$HOO^* + (H^+ + e^-) \rightarrow O^* + H_2O(l)$, (15)

$O^* + (H^+ + e^-) \rightarrow HO^*$, (16)

$HO^* + (H^+ + e^-) \rightarrow * + H_2O(l)$. (17)

Reaction 12 denotes the diffusion process of aqueous O_2 *via* the Nernstian diffusion layer, and the rate was computed by Haseen et al. [16] to be $8*10^5 \cdot S^{-1}$. The following step (Equation 13) stands for the adsorption of O_2 into the surface and the prefactor was considered as $1*10^8 \cdot S^{-1}$ due to the solvent reorganization to accommodate an O_2 molecule. Four consecutive proton-electron coupled processes for ORR are denoted by Equation 14 -Equation 17 among which the energy of proton-electron pair was referred to the energy of 1/2 H_2 in the CHE model [11]. For the O-O bond activation together with the protonation related to Equation 15, the data was from Ref. [18] where the subsequent reaction was based on the calculated G_a. Specifically, the data was recalculated to be $G_a = 0.8(G_{O*} - G_{HOO*}) + 1.35 + 0.42U$. For other reactions, we used an intrinsic barrier of 0.26 eV and considered that 0.5 electrons had transferred at the transition state [19]. Besides, the prefactors for all these proton-electron coupled transfer processes were fixed at $1*10^9 \cdot S^{-1}$ to compensate solvent reorganization [14]. The current density (*j*) of simulated ORR polarization curves is computed by the following equation:

$$j = e\rho TOF_{e^-}$$

in which, e is the elementary charge, ρ is density of surface-active sites, while TOF_{e^-} denotes the turnover frequency of electrons. Similarly, partial current densities of H_2O and H_2O_2 (denotes as *x*) can be computed by:

$$j_x = -2e\rho TOF_x$$

where the TOF values for the equations above are obtained by solving a set of ordinary differential equations (ODEs) together with the rate equations as stated in Ref. [16]. Or more straightforwardly, one can directly refer to the ORR example provided in CatMAP documentaions to solve ODEs.

In addition to the pH-dependent volcano plot for 4e$^-$ ORR, the pH-dependent volcano plot for H_2O_2 production is shown in **Figure S4**.

Table S1. Surface energies (eV) for different surfaces of ZrN.

Surface	100	001	011	110-1	110-2	111-1	111-2	120
Surface energy	–0.01	–0.01	0.04	0.04	0.04	0.05	0.05	0.03

Table S2. Comparison between different functionals (binding energies of O*, HO*, and HOO* on pristine ZrN(100) surface).

	RPBE	PBE
E_{O*} (eV)	-0.79	-0.81
E_{HO*} (eV)	-1.33	-1.43
E_{HOO*} (eV)	1.98	1.68

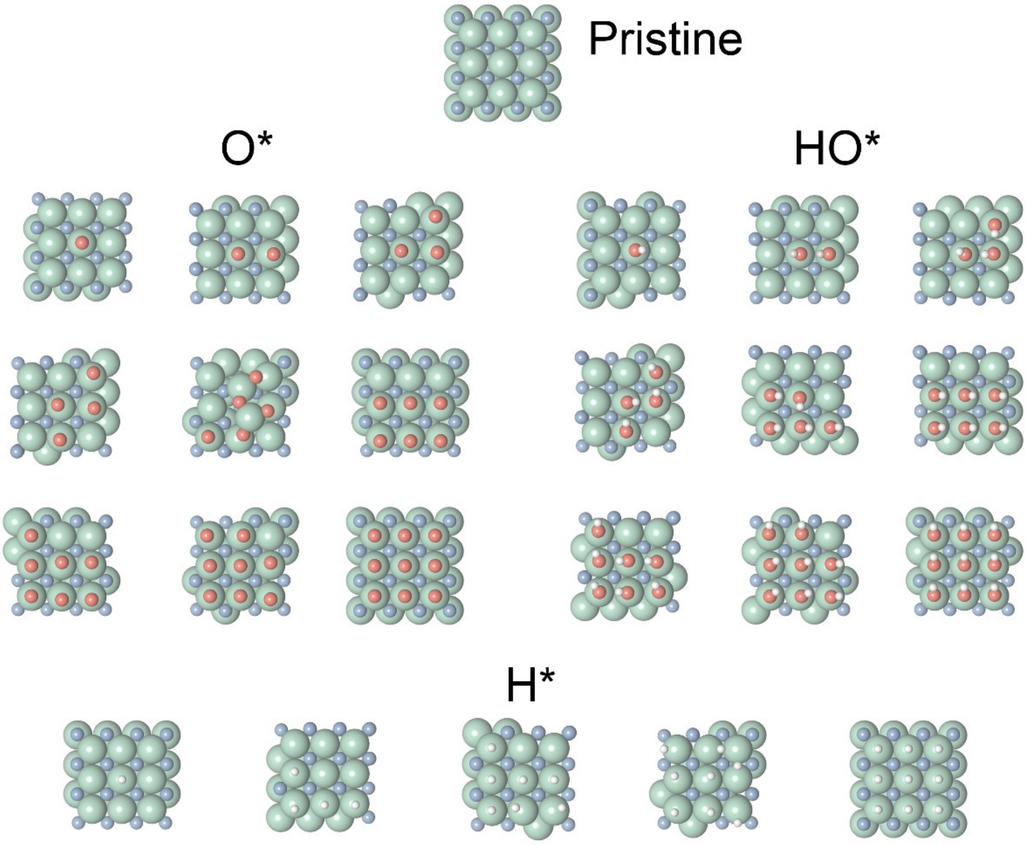

Figure S1. Atomic structures (top view) corresponding to different plots in **Figure 1a** in the maintext. Green, blue, red, and white spheres denote Zr, N, O, and H, respectively.

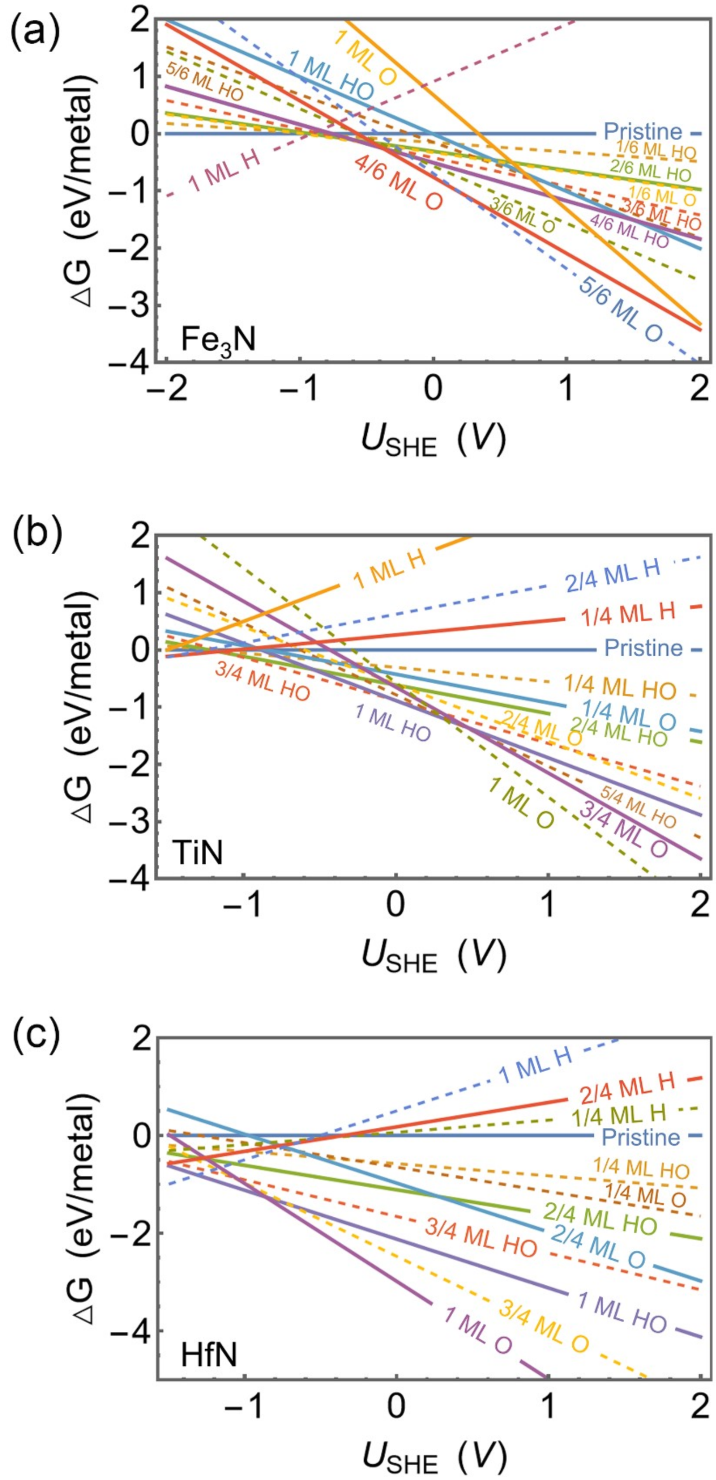

Figure S2. Calculated 1D surface Pourbaix diagrams as a function of potential *vs*. SHE (pH=13; T=298.15 K) for (a) Fe_3N(111), (b) TiN(100), and (c) HfN(100).

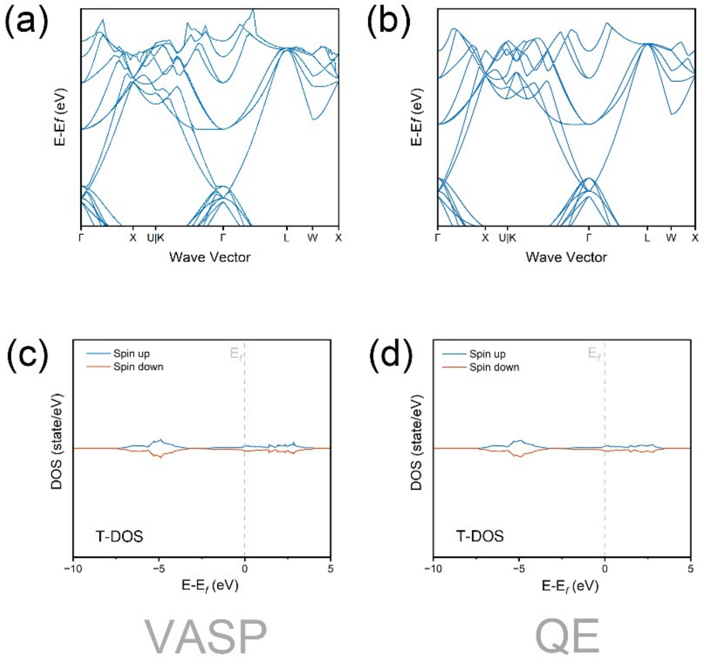

Figure S3. Band structure of bulk ZrN derived from (a) VASP and (b) Quantum Espresso; total density of states of bulk ZrN computed by (c) VASP and (d) Quantum Espresso.

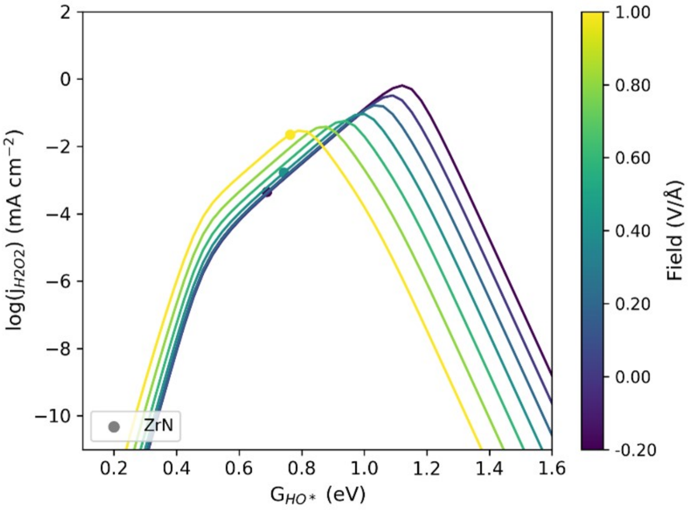

Figure S4. Derived pH-dependent volcano activity model for ORR towards H_2O_2 production as a function of HO* adsorption (at 0.6 V *vs*. RHE)

Reference

[1] J. Hafner, Ab-initio simulations of materials using VASP: Density-functional theory and beyond, J Comput Chem, 29 (2008) 2044-2078.

[2] P.E. Blochl, Projector augmented-wave method, Physical Review B, 50 (1994) 17953-17979.

[3] G. Kresse, J. Furthmuller, Efficient iterative schemes for ab initio total-energy calculations using a plane-wave basis set, Physical Review B, 54 (1996) 11169-11186.

[4] W. Kohn, L.J. Sham, Self-consistent equations including exchange and correlation effects, Physical Review, 140 (1965) 1133-&.

[5] J.P. Perdew, K. Burke, M. Ernzerhof, Generalized gradient approximation made simple, Physical Review Letters, 77 (1996) 3865-3868.

[6] B. Hammer, L.B. Hansen, J.K. Norskov, Improved adsorption energetics within density-functional theory using revised Perdew-Burke-Ernzerhof functionals, Physical Review B, 59 (1999) 7413-7421.

[7] H.J. Monkhorst, J.D. Pack, Special points for brillouin-zone integrations, Physical Review B, 13 (1976) 5188-5192.

[8] S.P. Ong, W.D. Richards, A. Jain, G. Hautier, M. Kocher, S. Cholia, D. Gunter, V.L. Chevrier, K.A. Persson, G. Ceder, Python Materials Genomics (pymatgen): A robust, open-source python library for materials analysis, Computational Materials Science, 68 (2013) 314-319.

[9] A.H. Larsen, J.J. Mortensen, J. Blomqvist, I.E. Castelli, R. Christensen, M. Dulak, J. Friis, M.N. Groves, B. Hammer, C. Hargus, E.D. Hermes, P.C. Jennings, P.B. Jensen, J. Kermode, J.R. Kitchin, E.L. Kolsbjerg, J. Kubal, K. Kaasbjerg, S. Lysgaard, J.B. Maronsson, T. Maxson, T. Olsen, L. Pastewka, A. Peterson, C. Rostgaard, J. Schiotz, O. Schutt, M. Strange, K.S. Thygesen, T. Vegge, L. Vilhelmsen, M. Walter, Z.H. Zeng, K.W. Jacobsen, The atomic simulation environment-a Python library for working with atoms, Journal of Physics-Condensed Matter, 29 (2017), 273002-273031.

[10] A. Jain, S.P. Ong, G. Hautier, W. Chen, W.D. Richards, S. Dacek, S. Cholia, D. Gunter, D. Skinner, G. Ceder, K.A. Persson, Commentary: The Materials Project: A

materials genome approach to accelerating materials innovation, Apl Materials, 1 (2013), 011002.

[11] J.K. Norskov, J. Rossmeisl, A. Logadottir, L. Lindqvist, J.R. Kitchin, T. Bligaard, H. Jonsson, Origin of the overpotential for oxygen reduction at a fuel-cell cathode, J. Phys. Chem. B, 108 (2004) 17886-17892.

[12] M. Bajdich, M. Garcia-Mota, A. Vojvodic, J.K. Norskov, A.T. Bell, Theoretical Investigation of the Activity of Cobalt Oxides for the Electrochemical Oxidation of Water, J. Am. Chem. Soc., 135 (2013) 13521-13530.

[13] J.A. Gauthier, C.F. Dickens, L.D. Chen, A.D. Doyle, J.K. Norskov, Solvation Effects for Oxygen Evolution Reaction Catalysis on IrO2(110), Journal of Physical Chemistry C, 121 (2017) 11455-11463.

[14] S.R. Kelly, C. Kirk, K. Chan, J.K. Nørskov, Electric Field Effects in Oxygen Reduction Kinetics: Rationalizing pH Dependence at the Pt(111), Au(111), and Au(100) Electrodes, The Journal of Physical Chemistry C, 124 (2020) 14581-14591.

[15] P. Giannozzi, S. Baroni, N. Bonini, M. Calandra, R. Car, C. Cavazzoni, D. Ceresoli, G.L. Chiarotti, M. Cococcioni, I. Dabo, A. Dal Corso, S. de Gironcoli, S. Fabris, G. Fratesi, R. Gebauer, U. Gerstmann, C. Gougoussis, A. Kokalj, M. Lazzeri, L. Martin-Samos, N. Marzari, F. Mauri, R. Mazzarello, S. Paolini, A. Pasquarello, L. Paulatto, C. Sbraccia, S. Scandolo, G. Sclauzero, A.P. Seitsonen, A. Smogunov, P. Umari, R.M. Wentzcovitch, QUANTUM ESPRESSO: a modular and open-source software project for quantum simulations of materials, J Phys Condens Matter, 21 (2009) 395502.

[16] H.A. Hansen, V. Viswanathan, J.K. Nørskov, Unifying Kinetic and Thermodynamic Analysis of 2 e– and 4 e– Reduction of Oxygen on Metal Surfaces, The Journal of Physical Chemistry C, 118 (2014) 6706-6718.

[17] A.J. Medford, C. Shi, M.J. Hoffmann, A.C. Lausche, S.R. Fitzgibbon, T. Bligaard, J.K. Nørskov, CatMAP: A Software Package for Descriptor-Based Microkinetic Mapping of Catalytic Trends, Catalysis Letters, 145 (2015) 794-807.

[18] C.F. Dickens, C. Kirk, J.K. Nørskov, Insights into the Electrochemical Oxygen Evolution Reaction with ab Initio Calculations and Microkinetic Modeling: Beyond the

Limiting Potential Volcano, The Journal of Physical Chemistry C, 123 (2019) 18960-18977.

[19] V. Tripkovic, T. Vegge, Potential- and Rate-Determining Step for Oxygen Reduction on Pt(111), Journal of Physical Chemistry C, 121 (2017) 26785-26793.